VILNIUS TECH
Vilnius Gediminas
Technical University

AVIATION

INVESTIGATION OF AERODYNAMIC CHARACTERISTICS OF SWEPT C-WING CONFIGURATIONS AT TRANSONIC SPEED USING DESIGN OF EXPERIMENTS AND COMPUTATIONAL FLUID DYNAMICS

Heershikesh Heerish SAMPUTH [1], Lip Kean MOEY [2]✉, Vin Cent TAI [2], Yong Chai TAN [2]

[1]Faculty of Engineering, Built Environment & Information Technology, SEGi University, 47810 Selangor, Malaysia
[2]Centre for Modelling and Simulation, Faculty of Engineering, Built Environment & Information Technology, SEGi University, 47810 Selangor, Malaysia

Abstract. Authors investigated the aerodynamic characteristics of backward swept (BSCW) and forward swept (FSCW) C-wing configurations at transonic speed using Design of Experiments (DoE) and Computational Fluid Dynamics (CFD), aiming to enhance aircraft performance. Five geometric parameters for C-winglet design were identified from the literature. A quarter fractional factorial approach for the DoE was employed to analyse the effect of these parameters on aerodynamic characteristics at a constant Mach number and angle of attack of 0.8395 and 3.06°, respectively. Numerical results confirm the accuracy of the regression model in predicting aerodynamic coefficients, while normal plot highlight influential geometric parameters. Retrofitting C-winglets at the wingtips increases the aerodynamic performance by approximately 9.38% and 9.74% for BSCW and FSCW configurations respectively, compared to wings without C-winglets. The study demonstrates that utilizing a large cant angle and sweep angle of 60°, along with a low taper ratio of 0.562 for both the vertical and horizontal winglets, as well as a low cant angle of 90° for the horizontal winglet, reduces shockwave interactions on the C-winglet surface, consequently leading to a reduction in drag. It was concluded that the geometric parameters of the C-winglet play an integral role in designing new aircraft aimed at reducing drag.

1. Introduction

After facing the challenges brought about by the COVID-19 pandemic, the long-term outlook for passenger traffic growth appears resilient. The International Air Transport Association (IATA) predicts that the demand for air travel will double by 2040, maintaining a consistent expansion at an average annual rate of 3.4% (International Air Transport Association, 2023). This forecast demonstrates an optimistic trajectory, considering the recovery efforts and the changing travel patterns expected post-pandemic. However, an increase in air travel demand will result in a rise in CO_2 emissions, with the aviation sector accounting for 2.5% of global CO_2 emissions, as reported by IATA (International Air Transport Association, 2023). In addition, previous study reported that by 2050, air travel will increase due to growth in the socio-economic sector, necessitating larger aircraft to accommodate the rising number of passengers (Grimme et al., 2021). Air transport remains the most important means of traveling from one destination to another in a shorter time, whether for leisure or cargo, compared to other existing modes of transporta-

tion. Therefore, the aviation industry is actively looking to develop new aircraft that offer high performance while minimizing environmental impact.

To meet the increasing demand for air travel, the aviation industry is actively pursuing the development of new aircraft capable of providing swift transportation without compromising performance or environmental sustainability. Most of these new aircraft must have the ability to travel at transonic speed, without affecting the aerodynamic efficiency of the aircraft. However, at transonic speed, aircraft experienced a rise in induced drag which is accounted for 40% of the total drag at cruising, and up to 80% to 90% of the total drag during take-off conditions (Coelho Barbosa, 2023; Guerrero et al., 2020; Hrúz et al., 2022; Kroo, 2005; Suresh et al., 2015). This resulted in more fuel consumption and causing an increase in CO_2 emission which was estimated to grow by 2.8% annually (Le Quéré et al., 2020). Therefore, non-planar wing configuration has been introduced onto the aircraft wing to reduce the drag by increasing the span efficiency factor also known as Oswald's factor (Kroo, 2005; Suresh et al., 2015).

The aerodynamic characteristics of winglets (Guerrero et al., 2020; Kazim et al., 2022; Whitcomb, 1976), C-wing (Gobpinaath et al., 2016; Suresh et al., 2015; Yahyaoui, 2019), and box wing (Gagnon & Zingg, 2016; Jemitola & Okonkwo, 2023; Sutthison et al., 2022; Yahyaoui, 2019) configurations were amongst the most studied non-planar wing configurations. Up to date, only winglets have been implemented in operational aircraft. Studies on winglets were conducted either in a wind tunnel experiment, analytical analysis or numerical analysis. The studies showed that winglet configurations have the ability to reduce the induced drag by 20% to 50% (Kehayas, 2021; Krishnan et al., 2020; Whitcomb, 1976). Nevertheless, wings with winglet configurations generally experienced shockwave interaction on the upper surface and this resulted in an increase in wave drag. Previous studies found that varying different geometrical parameters of a winglet can further improve the aerodynamic performance of an aircraft by reducing both induced drag and wave drag (Guerrero et al., 2020; Kazim et al., 2022). Moreover, Yahyaoui stated that vortex drag reduction was more important than increasing the lift to drag ratio (C_L/C_D) of the wing configuration because vortex drag constituted a significantly larger portion of the total drag of an aircraft compared to the profile drag solely caused by the wings (Yahyaoui, 2019). Additionally, this study demonstrated that incorporating both stagger and moderate sweep provide a slight advantage to the C-wing and wing with winglet configurations compared to the box wing configuration in terms of the span efficiency factor (Yahyaoui, 2019). Furthermore, the C-wing configurations have almost the same drag reduction effect on large-wetted areas as the box wing and winglet configurations at subsonic speed. Hence, retrofitting the C-wing configuration onto the existing wing will be easier to implement compared to the box wing configuration.

Moreover, the C-wing configuration has the ability to increase aerodynamic performance, usually measured in terms of C_L/C_D. Suresh et al. investigated the C_L/C_D between a C-wing configuration and straight wing configuration on a commercial aircraft at a Mach number of 0.85 while varying the angle of attack (AoA) from 0° to 4° (Suresh et al., 2015). The study found that the C-wing configuration has a higher C_L/C_D than the straight wing configuration, and the same goes for the drag coefficient (C_D). The reason for the C-wing configuration having a high C_D was due to the additional surfaces which caused an increase in parasite drag. Nevertheless, the C-wing configuration increased the lift coefficient (C_L). Furthermore, as mentioned earlier, wave drag is another factor that can affect the aerodynamic performance of the C-wing configuration, especially at transonic speed, due to its similarity to the winglet configuration, leading to shockwave interaction. Shockwave interaction is typically caused by the collision or convergence of multiple shockwaves, often occurring at the junction of two or more bodies. For instance, Guerrero et al. (2020) described this phenomenon in the context of a wing with winglets, and the same can be observed in the case of the C-wing configuration (Guerrero et al., 2020). However, previous studies have investigated the effect of aerodynamic characteristics, such as aerodynamic performance and shockwave interaction, but have not considered simultaneously varying multiple geometry parameters of C-wing configurations at transonic speed. Therefore, designing a C-wing configuration at transonic speed will require a comprehensive study to understand the aerodynamic characteristics while considering the geometry of the wing.

The aim of study was to employ both Design of Experiments (DoE) and Computational Fluid Dynamics (CFD) to investigate the aerodynamic characteristics of swept configurations with varying the geometry of the C-winglet at transonic speed. Section 2 explains the methodology for this paper. Section 3 provides the numerical results as well as the discussion of the results obtained. Lastly, the paper concludes with a summary of findings and offers insights for future recommendations.

2. Problem description

2.1. Description of the wing geometry

The main wing surface was an ONERA M6 swept wing constructed based on the geometric parameters described by Schmitt (Schmitt, 1979) with a sweep angle of 30° and −30° for the backward swept wing (BSW) and forward swept wing (FSW), respectively. The geometric parameters chosen for constructing the C-winglet configuration are listed in Table 1, drawing from previous research that focused on either theoretical or experimental approaches. Figure 1 illustrates the geometric parameters of the backward swept C-wing (BSCW) and forward swept C-wing (FSCW). However, both the span of the vertical and horizontal winglet was kept at 20% of the semi-wingspan (b/2).

Table 1. Description of geometric parameters for the C-winglet

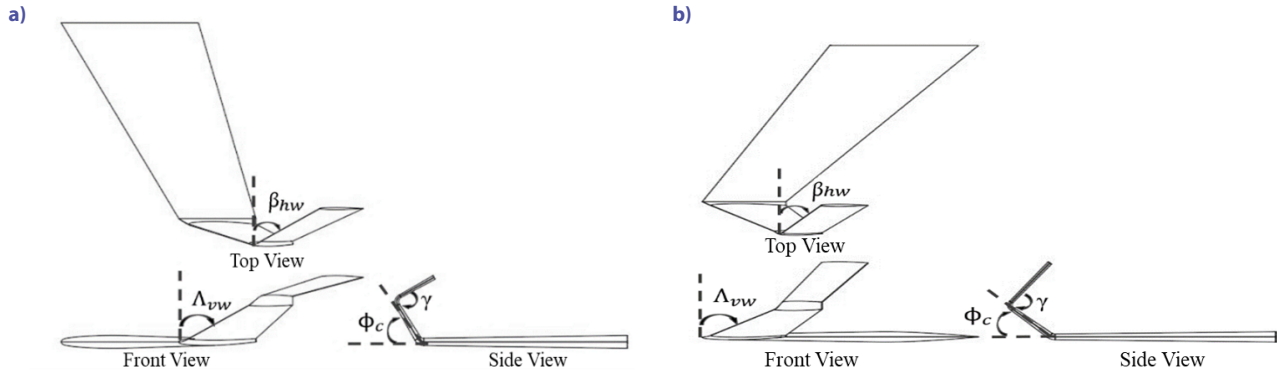| Factor	Geometric parameter	Low bound	High bound	Reference
A	Cant angle (ϕ_c)	45°	60°	(Guerrero et al., 2020)
B	Sweep angle of vertical winglet (Λ_{vw})	45°	60°	(Guerrero et al., 2018)
C	Angle between the vertical winglet and horizontal winglet (γ)	90°	100°	(Gobpinaath et al., 2016)
D	Sweep angle of horizontal winglet (β_{hw})	45°	60°	(Bikkannavar & Scholz, 2016)
E	Taper ratio of C-winglet (λ_{CWt})	0.562	1.0	(Yahyaoui, 2019)

Figure 1. Geometric parameters: (a) BSCW configuration; (b) FSCW configuration

2.2. Computational domain and boundary conditions

The computational domain was constructed by having a semi hemisphere of diameter 24 m drawn at the center of the leading edge of the airfoil at the wing root chord. In addition, a body of influence was constructed and extruded around the wing model. The benefit of having a body of influence around the model is it helped to ease the mesh transition. Figure 2 depicts the computational domain and boundary conditions, and Table 2 summarizes the boundary type and operating conditions that were employed in the study. The wing surface was a boundary wall type, modelled as a stationary adiabatic wall with a no-slip condition. The Riemann boundary condition was implemented for the far-field (Balan et al., 2020).
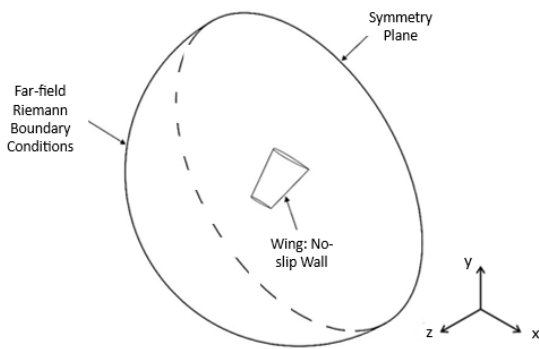

Figure 2. Computational domain and boundary conditions (not to scale)

Table 2. Summary of the boundary conditions

Parameters	Boundary type	Operating conditions
Far-field	Pressure Far-field	Mach Number (Ma) = 0.8395 Pressure (P) = 0 Pa Angle of attack (AoA) = 3.06° Temperature (T) = 300 K
Symmetry	Symmetry	Symmetry boundary
Wing surface	Wall	Stationary wall No slip condition

2.3. Description of numerical settings

The numerical simulations were carried out using ANSYS 2022R2. An unstructured poly-hexcore was used to discretize the computational domain of all four wing configurations. The Spalart-Allmaras turbulence model was employed to model the turbulent flow at steady state (Rumsey & Vatsa, 1995).The air was modelled as ideal gas with density of 1.177 kg/m^3 at operating pressure (P) and temperature (T) of 0 Pa and 300 K, respectively (Guerrero et al., 2018). The dynamics viscosity (μ) followed the three-coefficient Sutherland equation as given by Equation (1):

$$\mu = \mu_o \left(\frac{T}{T_o} \right)^{\frac{3}{2}} \frac{T_o + S}{T + S},\tag{1}$$

where the reference viscosity, μ_0 = 1.716×10^{-5} kg/m·s, reference temperature, T_0 = 273.11 K, and Sutherland constant, S = 110.56 K. The reference area value used was 0.7532 m^2 (Schmitt, 1979). A SIMPLE algorithm was chosen for the Pressure-Velocity Coupling. Least Squares Cell Based (LSCB) was used for the gradient reconstruction method with a combination of second order pressure interpolation and second order upwind discretization schemes applied to the viscous terms of the governing equation. The convergence study was accelerated by enabling the Pseudo-transient implicit, Warped- Face Gradient Correction (WFGC), High Order Term Relaxation (HOTR) under-relaxation method. A hybrid initialization was adopted. The convergence criterion for the residual attained a level of 1×10^{-6} for continuity,1×10^{-9} for x, y, and z velocities, 1×10^{-9} for energy, 1×10^{-8} for nut.

2.4. Mesh convergence study

The mesh convergence study was performed on the BSW configuration at 3.06˚ AoA to accurately predict the aerodynamic coefficients. During the study, four different meshes were created on the wing surface with different surface mesh, average y+, growth rate and prismatic layer, as listed in Table 3. The meshes 1 to 4 were categorized as coarse, medium, fine, and very fine, respectively.

Table 3. Surface mesh used in this study

Type of Mesh	Surface mesh	y+ average	Growth rate	Prismatic layer
Mesh 1: Coarse	1439040	≈ 29	1.2	10
Mesh 2: Medium	3829438	≈ 2.3	1.175	20
Mesh 3: Fine	4654765	≈ 2.4	1.15	22
Mesh 4: Very fine	18111261	≈ 2.1	1.125	34

Figure 3 shows the C_L and C_D of the four meshes and their Richardson extrapolation values. The Richardson extrapolation values were computed using the finer meshes (mesh 3 and mesh 4). To compute these values, Equation (2) was used with a mesh refinement ratio r equal to 1.6 and an order of convergence p equal to 2 as presented in (Guerrero et al., 2020). In Equation (2), f_1 represents the finer mesh which is mesh 4 while f_2 represents the coarser mesh which is mesh 3 for this study. The results appear to be approaching nearly the same results as the mesh was refined.
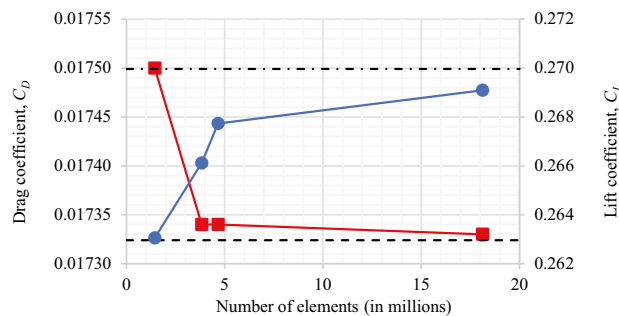
$$f_{h=0} \cong f_1 + \frac{f_1 - f_2}{r^p - 1}. \tag{2}$$

Figure 3. Mesh convergence study for C_D and C_L is represented by the red and blue solid lines, respectively. The Richardson extrapolation for the C_D and C_L is depicted by the dashed line and dashed dotted line, respectively

Table 4. Difference of the C_L and C_D between the meshes

QOI	C_L	C_D
Outcome of mesh 4	0.26909	0.01733
Richardson extrapolation, $f_{h=0}$	0.26996	0.01732

Table 4 lists the outcome of the quality of interest (QOI) of mesh 4 and the Richardson extrapolation value. The Richardson extrapolation was computed using mesh 3 and mesh 4. The deviation between the outcome of mesh 4 and Richardson extrapolation was approximately 0.32% and 0.04% for C_L and C_D, respectively.

In Table 5, the percentage changes between meshes 1–4 and the Richardson extrapolation, as well as between meshes 1–3 and mesh 4 were listed as PC_1 and PC_2, respectively. The values of PC_1 for both aerodynamic coefficients were computed using Equation (3), where $f_{h=0}$ represents the value obtained for the Richardson extrapolation and f_m represents the outcome of meshes 1–4 for both C_L and C_D. The values of PC_2 for C_L and C_D were calculated by subtracting the values of the finer mesh (mesh 4) from those of the coarse meshes (mesh 1–3). The results revealed that increasing the mesh refinement, the discrepancies between the findings of this study and the Richardson extrapolation, become smaller. This indicates an improvement in the accuracy of the simulations as the mesh was refined. Therefore, based on the result presented in Table 5, the fine mesh (mesh 3) was retained for subsequent simulations due to low computational time and, the deviation between the mesh 4 and mesh 3 was approximately 0.504% and 0.058% for C_L and C_D, respectively.

$$PC_1 \cong \left(\frac{f_{h=0} - f_m}{f_{h=0}} \right) \times 100\%. \tag{3}$$

2.5. Model validation

A model validation was conducted for the BSW configuration, comparing the pressure coefficient (C_p) distribution of the CFD result with experimental data from the previous study (Schmitt, 1979). This comparison was plotted across seven stations of wingspan at z/(b/2) = 0.2, 0.44, 0.65, 0.80, 0.90, 0.95, and 0.99 as illustrated in Figure 4. The experimental conditions used for comparison with the CFD results were obtained from Test Case 2308, which had a Mach number, AoA, and Reynolds number of 0.8395, 3.06°, and 11.72×10^6, respectively (Schmitt, 1979). Additionally, the Relative Root Mean Square Error (RRMSE) was employed to validate the model. It assessed the accuracy between the obtained CFD result and the experiment data of the C_p plot data. The RRMSE is obtained using Equation (4) (Zhou et al., 2016).

Table 5. Difference of the C_L and C_D between the type of meshes

Type of Mesh	C_L	C_D	C_L PC_1	C_D PC_1	C_L PC_2	C_D PC_2
Mesh 1: Coarse	0.26305	0.01750	2.56029	−1.01832	−2.23735	0.98132
Mesh 2: Medium	0.26612	0.01734	1.42309	−0.09473	−1.10016	0.05772
Mesh 3: Fine	0.26773	0.01734	0.82671	−0.09473	−0.50377	0.05772
Mesh 4: Very fine	0.26909	0.01733	0.32293	−0.03700	−	−

Note: PC_1 represents the percentage change computed between the mesh outcome for meshes 1–4 and the Richardson extrapolation value.
PC_2 represents the percentage change calculated between the outcomes of meshes 1–3 and mesh 4.

$$RRMSE = \frac{\sqrt{\frac{1}{n}\sum_{i=1}^{n}\left(C_{p_{Experimental}} - C_{p_{CFD}}\right)^2}}{\sum_{i=1}^{n}C_{p_{Experimental}}} \times 100, \quad (4)$$

where C_{pCFD} represents the pressure coefficient obtained from the CFD results using the Spalart-Allmaras (one equation) turbulence model, meanwhile $C_{pExperimental}$ represents the pressure coefficient obtained from wind tunnel experiment published by Schmitt (Schmitt, 1979). The RRMSE values obtained with mesh 3 are as follows: 1.69%, 0.75%, 2.81%, 3.39%, 2.61%, 1.91%, and 2.52% for z/(b/2) = 0.2, 0.44, 0.65, 0.8, 0.9, 0.95, and 0.99, respectively. The obtained RRMSE values, indicate a closer agreement between the CFD simulation and experimental data, suggesting smaller discrepancies. Additionally, the average

RRMSE value across the seven stations is 2.24%. This indicates excellent model accuracy, as it is below the threshold of 10% (Li et al., 2013). Based on the result obtained from the RRMSE, it confirms that the C_p distribution plot of both CFD result and experimental data exhibit a similar trend. Moreover, the expected double lambda shock on the suction side of the wing is effectively captured, as depicted in Figure 5. Moving from the inboard section to the outboard section, the double lambda shock (refer to Figures 5a to 5c) transitions into a single shock (refer to Figures 5d to 5e) positioned closer to the leading edge. Minor discrepancies observed between the CFD and experimental results might be attributed to the wing models utilized: the experiment employed a wing model with a sharp trailing edge, while the CFD study employed a wing model featuring a blunt trailing edge.
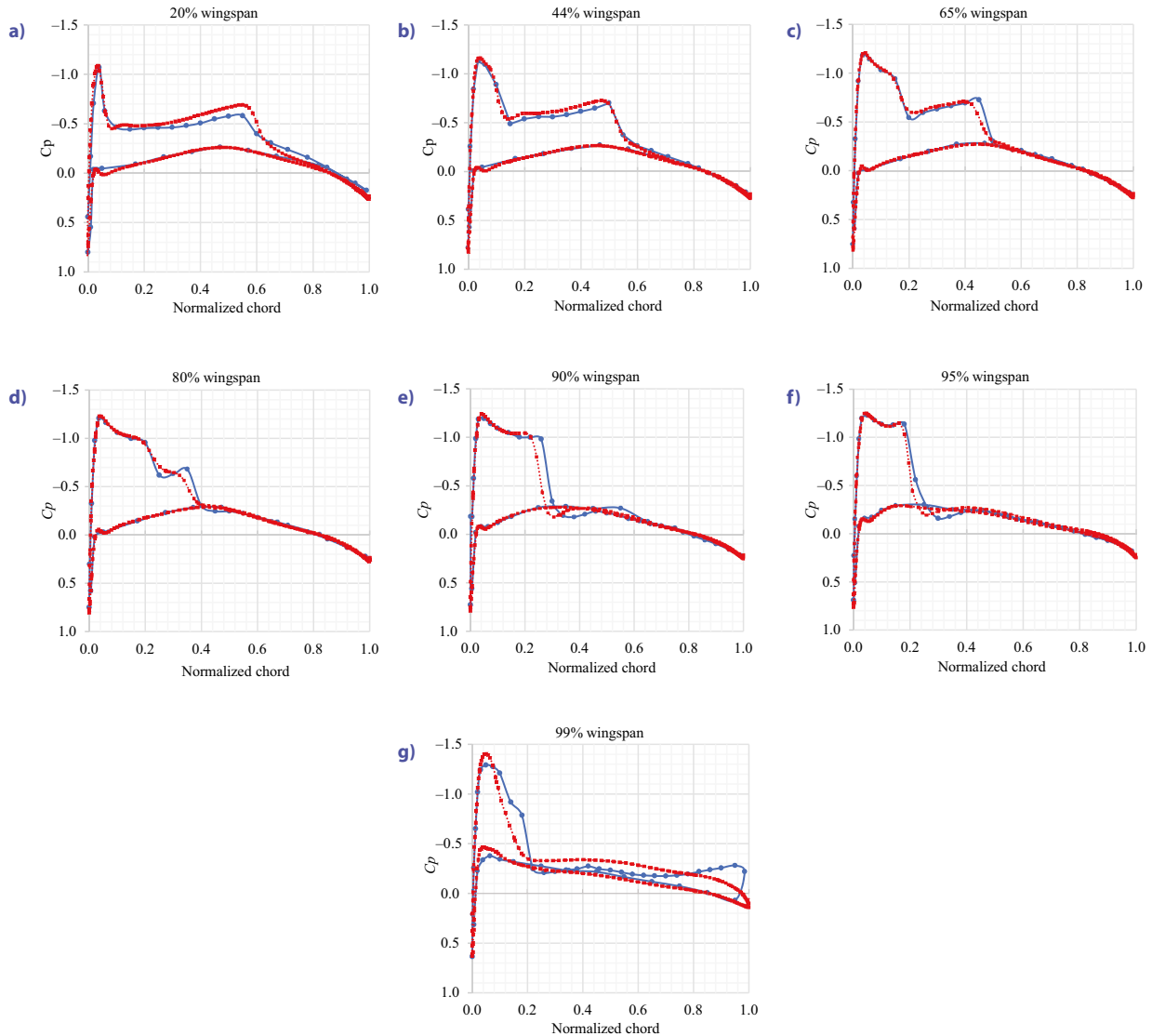

Figure 4. Comparison of CFD result (Red dotted line) and Experimental data (Schmitt, 1979) (Blue solid line) in terms of *Cp* along the wingspan located at: (a) 20%; (b) 44%; (c) 65%; (d) 80%; (e) 90%; (f) 95%; (g) 99%
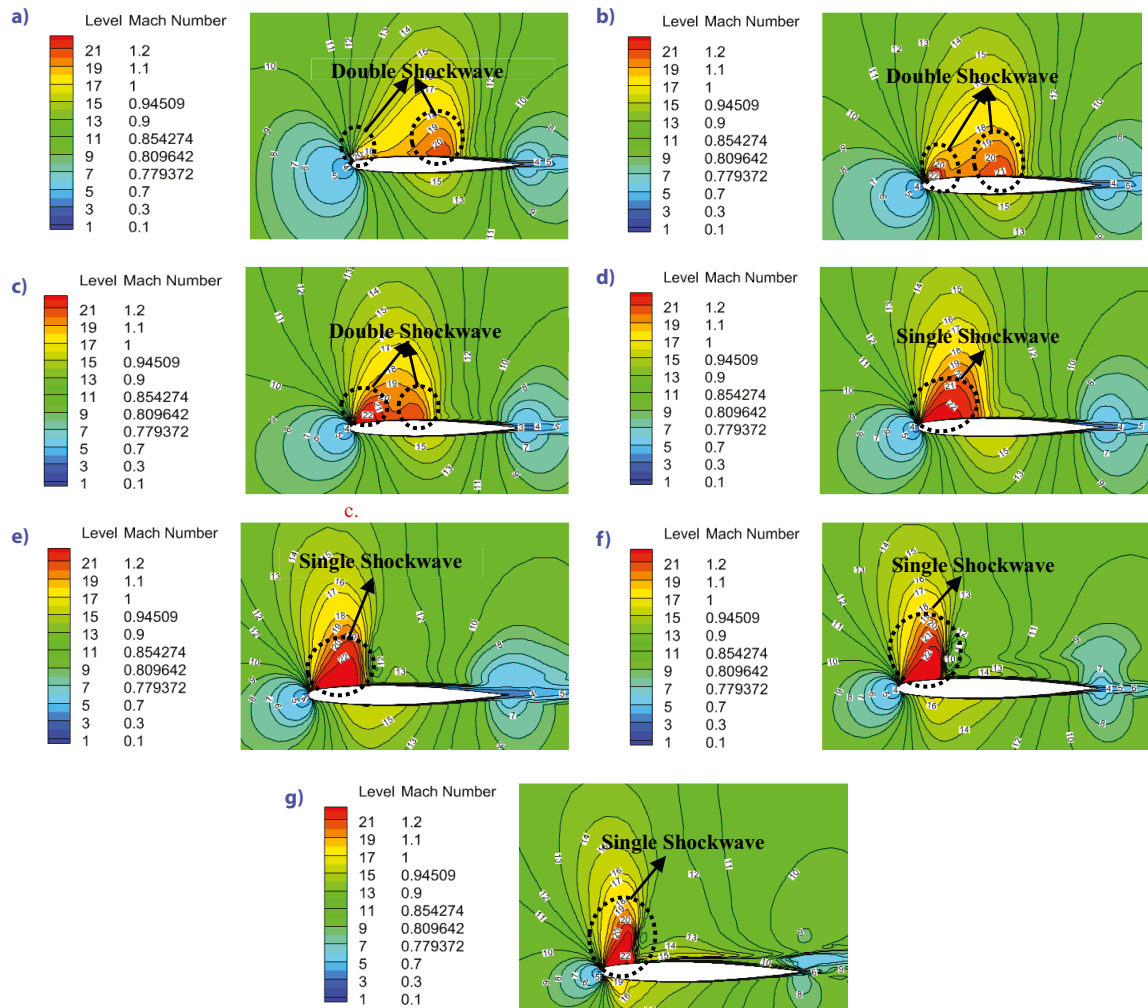
Figure 5. Mach number contours of the back swept wing configuration along the wingspan located at: (a) 20%; (b) 44%; (c) 65%; (d) 80%; (e) 90%; (f) 95%; (g) 99%

2.6. Design of experiment method

A ¼ fractional factorial of a resolution III design was utilized for the Design of Experiment (DoE) method (Antony, 2023; Das & Dewanjee, 2018) to analyse the influence of each factor and their interactions on the response variables: lift coefficient (C_L), drag coefficient (C_D), and lift to drag (C_L/C_D) for the C-wing design. The ¼ fractional factorial design belonged to the broader category of fractional factorial designs within experimental statistics. It is employed to investigate the impact of k independent factors, each varying at 2 levels, on the response variable. The ¼ designation indicates that this design utilized just one-quarter of the total experimental runs needed for a complete factorial experiment. For instance, in a full factorial design with 5 factors, each at 2 levels, 32 runs were conducted, whereas a ¼ fractional design would require only 8 experiments. Fractional factorial designs offered significant advantages in managing high-factor scenarios and resource constraints while retaining critical interaction information. They played a crucial role in preliminary

studies, identifying influential factors for focused analysis. However, limitations arise concerning confounding effects in higher-order interactions, making factor distinction challenging. Resolution, which helps understand how factors interact, shows that higher resolution designs can figure out complex interactions but need more experiments. For this study, a resolution III design was employed to the fractional factorial their balance between studying individual factors independently and the limitations of available resources like time, cost, or experimental capacity. A resolution III design is where the main effects (individual factors) are not confounded with each other but are confounded with two-factor interactions (Antony, 2023).

In this study, MINITAB 20 is used to generate the factorial points and perform the DoE analysis. From ¼ fractional factorial, eight distinctive configurations have been generated with a variation of low and high bounds of each factor for both the BSCW and FSCW configurations as tabulated in Table 6. Subsequently, each of the eight configurations of the respective C-wing configurations were numerically analysed and the response variables were collected. The

Table 6. Description of BSCW and FSCW configurations for DoE

Config No.	Factor A, [°]	Factor B, [°]	Factor C, [°]	Factor D, [°]	Factor E
1	45	45	90	60	1.0
2	60	45	90	45	0.562
3	45	60	90	45	1.0
4	60	60	90	60	0.562
5	45	45	100	60	0.562
6	60	45	100	45	1.0
7	45	60	100	45	0.562
8	60	60	100	60	1.0

collected data of the response variables were subjected to the regression modelling where a stepwise regression method was employed. The implementation of a stepwise regression aimed to improve the model fit by systematically adding or removing factors based on their statistical significance. In addition, a default criterion of 0.15 alpha was adopted for significance level. The stepwise regression equation is given as:

$$Y = \beta_0 + \beta_1 X_1 + \beta_2 X_2 + \beta_3 X_1 X_2 + \ldots + \beta_k X_k + \epsilon . \qquad (5)$$

In Equation (5), the relationship between the geometric factors and the response variables: C_L, C_D, and C_L/C_D are represented by the response model, Y. The intercept term is denoted by β_0, which is the baseline level of the response when all factor X_1, X_2, ..., X_k are zero. The terms β_1, β_2, ...,β_k are the model coefficients for the main effects of factors X_1, X_2, ..., X_k, respectively. The term $X_1 X_2$ represents the interaction effects between the factors X_1 and X_2. Finally, ϵ represents the random error term, describing the uncertainty or unexplained variability in the model.

3. Result and discussion

3.1. Design of Experiment (DoE) results

Table 7 presents the correlation of coefficient (R^2) and regression equations for C_L, C_D, and C_L/C_D responses model in uncoded unit for both BSCW and FSCW configurations

at Ma = 0.8395 and 3.06° AoA. The results demonstrate that that the C_{Lr} and C_{Dr} of both BSCW and FSCW configurations yield R^2 values ranging from 99.1% to 99.6%. Additionally, the C_{Lr}/C_{Dr} indicates that FSCW configurations exhibit an R^2 value of 11.4% higher than that of the BSCW configurations Therefore, it can be concluded that the responses can be effectively represented by the regression equations for both BSCW and FSCW configurations. Furthermore, to validate the accuracy and reliability of the regression equations in predicting the chosen response outcomes a comparison between the simulation result and regression result is carried out as detailed in Table 8 and Table 9 for both BSCW and FSCW configurations, respectively. The observed small percentage difference of around 1% between the simulation and regression results highlights the significance of geometric parameters in the regression model for optimizing aerodynamic features of the C-winglet. This suggests that the inclusion of geometric parameters in the regression model can be instrumental in further optimizing the C_L, C_D, and C_L/C_D characteristics of a given C-winglet.

Figure 6a and 6b display the normal plot of the standardized effects of the C_L response model for both BSCW and FSCW configurations. The normal plot of the standardized effects confirms that three main factors are significant for the BSCW configurations, while four main factors are significant for the FSCW configurations. The normal plot results show that factor B exhibits the most influence on C_L, while factor A is ranked second, followed by factor E in both configurations. However, the FSCW configuration involves an additional interaction factor, BE, which has the least influence on C_L. Additionally, factors B, A, E, and the BE interaction are inversely correlated with C_L, suggesting that an increase in the factor level will result in a decrease in C_L.

Figure 7a and 7b display the normal plot of the standardized effects of the C_D response model for both BSCW and FSCW configurations. The normal plot of the standardized effects confirms that three main factors are significant for the BSCW configurations, while four main factors are significant for the FSCW configurations. From the normal plot, factor B exhibits the most influence on C_D in

Table 7. Regression model analysis for the BSCW and FSCW configurations at Ma = 0.8395 and 3.06° AoA

Configuration	Response	Regression model analysis	
		R^2	Regression equation
BSCW	C_{Lr}	99.6%	$0.53816 - 0.001362\varphi_c - 0.001915\Lambda_{vw} - 0.02001\lambda_{cwt}$
	C_{Dr}	99.3%	$0.029672 - 0.000077\varphi_c - 0.000120\Lambda_{vw} + 0.000017\gamma$
	C_{Lr}/C_{Dr}	82.1%	$17.337 - 0.733\lambda_{cwt}$
FSCW	C_{Lr}	99.1%	$0.3226 - 0.000905\varphi_c - 0.000424\Lambda_{vw} + 0.0515\lambda_{cwt} - 0.001234\Lambda_{vw}*\lambda_{cwt}$
	C_{Dr}	99.2%	$0.039123 - 0.000035\varphi_c - 0.000164\Lambda_{vw} - 0.000048\beta_{hw} + 0.000912\lambda_{cwt}$
	C_{Lr}/C_{Dr}	93.5%	$10.058 - 0.02131\varphi_c + 0.01355\beta_{hw} - 0.809\lambda_{cwt}$

Note: Cant angle (φ_c), Sweep angle of vertical winglet (Λ_{vw}), Angle between the vertical winglet and horizontal winglet (γ), Sweep angle of horizontal winglet (β_{hw}), Taper ratio of C-winglet (λ_{cwt}).

both configurations. Factor A is ranked as the second most influential for C_D in the BSCW configurations, while it is ranked third for the FSCW configurations. For the FSCW configurations, factor D is the second most influential for C_D. Factor C is the least influential for the BSCW configuration, and factor E is the least influential for the FSCW configuration. Moreover, factors B, A, and D are inversely correlated with C_D, suggesting that an increase in their levels will result in a decrease in C_D. However, factors C and E have a positive effect on C_D, indicating that an increase in their levels will lead to an increase in C_D.

Figure 8a and 8b display the normal plot of the standardized effects of the C_L/C_D response model for both BSCW and FSCW configurations. The normal plot of the

Table 8. Percentage difference between the simulation and regression results for the BSCW configurations in terms of C_D, C_L, and C_L/C_D at Ma = 0.8395 and 3.06° AoA

Config No.	Simulation result			Regression result			% Difference		
	C_L	C_D	C_L/C_D	C_{Lr}	C_{Dr}	C_{Lr}/C_{Dr}	C_L	C_D	C_L/C_D
1	0.3706	0.0222	16.7128	0.3707	0.0223	16.6040	0.0229	0.6171	0.6510
2	0.3580	0.0212	16.8903	0.3590	0.0212	16.9251	0.2847	0.0849	0.2053
3	0.3407	0.0205	16.6158	0.3420	0.0205	16.6040	0.3698	0.1805	0.0710
4	0.3300	0.0194	16.9907	0.3303	0.0194	16.9251	0.0891	0.0928	0.3864
5	0.3811	0.0226	16.8284	0.3794	0.0225	16.9251	0.4454	0.4115	0.5744
6	0.3497	0.0212	16.4867	0.3503	0.0214	16.6040	0.1584	0.7170	0.7115
7	0.3505	0.0206	16.9900	0.3507	0.0207	16.9251	0.0640	0.5194	0.3823
8	0.3235	0.0195	16.6005	0.3215	0.0196	16.6040	0.6090	0.2667	0.0211

Note: All values were round off to 4 decimal places.

Table 9. Percentage difference between the simulation and regression results for the FSCW configurations in terms of C_L, C_D and C_L/C_D at Ma = 0.8395 and 3.06° AoA

Config No.	Simulation result			Regression result			% Difference		
	C_L	C_D	C_L/C_D	C_{Lr}	C_{Dr}	C_{Lr}/C_{Dr}	C_L	C_D	C_L/C_D
1	0.2580	0.0282	9.1497	0.2579	0.0282	9.0996	0.0368	0.0355	0.5476
2	0.2471	0.0279	8.8641	0.2463	0.0280	8.9314	0.3271	0.3509	0.7592
3	0.2326	0.0264	8.8237	0.2329	0.0265	8.8955	0.1161	0.3030	0.8137
4	0.2280	0.0248	9.1802	0.2289	0.0248	9.1356	0.4139	0.0722	0.4858
5	0.2612	0.0279	9.3789	0.2622	0.0278	9.4566	0.3758	0.4018	0.8285
6	0.2461	0.0286	8.6060	0.2465	0.0284	8.5745	0.1605	0.6993	0.3660
7	0.2457	0.0263	9.3528	0.2448	0.0261	9.2524	0.3526	0.8445	1.0735
8	0.2216	0.0253	8.7627	0.2215	0.0252	8.7786	0.0632	0.3162	0.1815

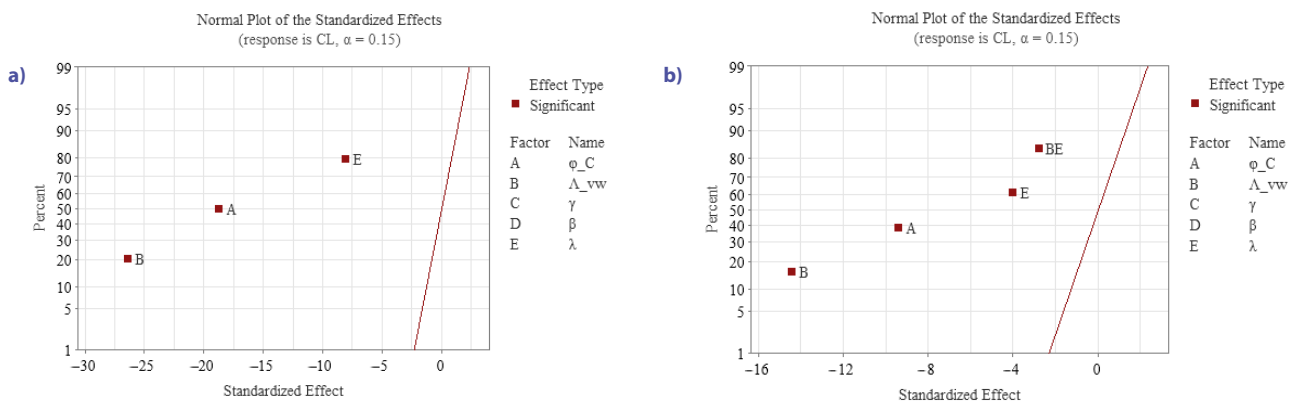*Note:* All values were round off to 4 decimal places.

Figure 6. Normal plot of the standardized effects for the response C_L at Ma = 0.8395 and 3.06° AoA: (a) BSCW configuration; (b) FSCW configuration
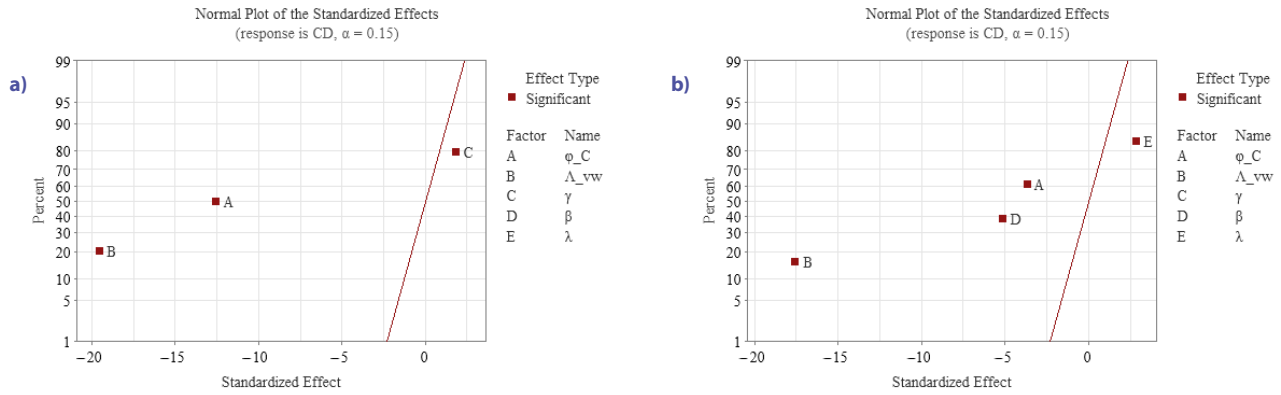
Figure 7. Normal plot of the standardized effects for the response C_D at Ma = 0.8395 and 3.06° AoA: (a) BSCW configuration; (b) FSCW configuration
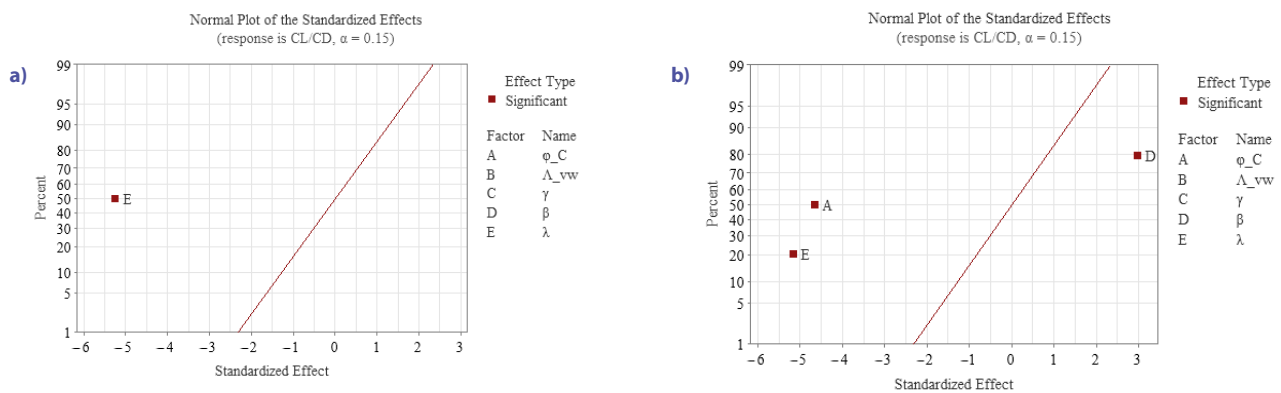

Figure 8. Normal plot of the standardized effects for the response C_L/C_D at Ma = 0.8395 and 3.06° AoA: (a) BSCW configuration; (b) FSCW configuration

standardized effects confirms that only one main factor is significant for the BSCW configurations, while three main factors are significant for the FSCW configurations. From the normal plot, factor E exhibits the most influence on C_L/C_D in both configurations. Factor A is ranked as the second most influential on C_L/C_D, followed by factor D for the FSCW configurations. In the normal plot for both C-wing configurations, factors E and A are inversely correlated with C_L/C_D suggesting that an increase in their levels will result in a decrease in C_L/C_D. In contrast, an increase in the level of factor D will lead to an increase in C_L/C_D.

3.2. Aerodynamic performance at 3.06° angle of attack

The aerodynamic performance is measured in terms of C_L/C_D at a constant 0.8395 Mach number and 3.06° AoA. A comparison was conducted between backward swept and forward swept configurations, both with and without the C-winglet as illustrated in Figure 9. The eight configurations of the BSCW and FSCW show an average increase of approximately 9.38% and 9.74% in the C_L/C_D, respectively compared to BSW and FSW configurations. The C_L/C_D values recorded for the BSW and FSW configurations were 15.1901 and 8.1291, respectively. Table 10 presents the lowest and highest aerodynamic performance record-

ed among the eight configurations of each swept C-wing configurations. The result shows that Configuration 4 exhibits the highest aerodynamic performance for the BSCW configuration with a C_L/C_D of 16.9907, while Configuration 5 shows the highest performance for the FSCW configuration with a C_L/C_D of 9.3789. On the other hand, Configuration 6 displays the lowest aerodynamic performance in both BSCW and FSCW configurations, with C_L/C_D values of 16.4867 and 8.6060, respectively. Therefore, retrofitting a C-winglet at the wingtip enhances the aerodynamic performance of the aircraft, regardless of the swept wing configuration used.
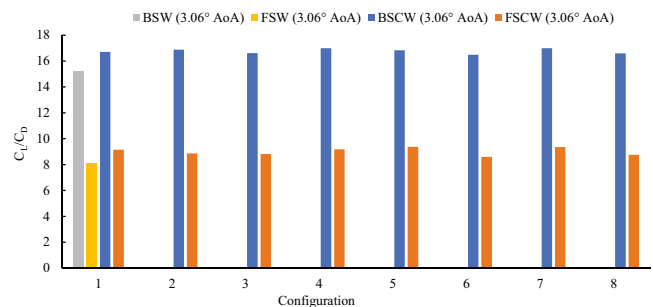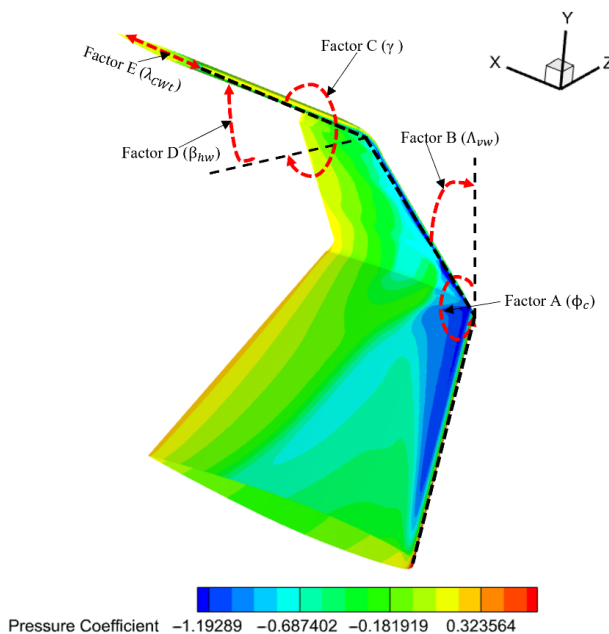

Figure 9. Comparison of C_L/C_D for the BSW, FSW, BSCW and FSCW configurations at Ma = 0.8395 and 3.06° AoA

Table 10. Aerodynamic performance between the C-wing configurations at Ma = 0.8395 and 3.06° AoA

Configuration	Low performance	High performance
BSCW	Configuration 6	Configuration 4
	C_L = 0.3497 C_D = 0.0212 C_L/C_D = 16.4867	C_L = 0.3300 C_D = 0.0194 C_L/C_D = 16.9907
FSCW	Configuration 6	Configuration 5
	C_L = 0.2461 C_D = 0.0286 C_L/C_D = 8.6060	C_L = 0.2612 C_D = 0.0279 C_L/C_D = 9.3789

Table 11. Geometric parameters used for the C-wing of backward and forward swept wing configurations

Config No.	Factor A, [°]	Factor B, [°]	Factor C, [°]	Factor D, [°]	Factor E
4	60	60	90	60	0.562
5	45	45	100	60	0.562
6	60	45	100	45	1.0

Table 12. Lowest and highest C_D for BSCW and FSCW configurations

Configuration	Lowest C_D	Highest C_D
BSCW	Configuration 4 C_D = 0.0194	Configuration 5 C_D = 0.0226
FSCW	Configuration 4 C_D = 0.0248	Configuration 6 C_D = 0.0286

3.3. Shockwave interaction on C-wing configurations at 3.06° angle of attack

Figure 10 shows the geometric parameters used for both BSCW and FSCW configurations. The interaction of shockwaves occurs when the shockwave generated by the main wing interacts with the surface of the C-winglet, resulting in an increase in drag. In this study, the system investigating shockwave interaction developed for BSCW and FSCW configurations at a 3.06° AoA is termed the Wing with C-winglet Shockwave Interaction (WCSWI). The WCSWI is divided into two sections known as the Main Wing with Vertical Winglet Shockwave Interaction (MWVWSWI) and the Vertical and Horizontal Winglet Shockwave Interaction (VWHWSWI). The WCSWI can be computed by employing either the pressure coefficient contour plot or the Q-criterion method. In the pressure coefficient contour plot, the dark blue region on the wing surface indicates a low-pres-

sure area, suggesting shockwave formation or increased drag, which, in turn, may imply the presence of high stress gradients. The Q-criterion method used to investigate the shockwave interaction is measured in term of Mach number at a level of 0.001. Table 11 presents the geometric parameters for the considered BSCW and FSCW configurations used in the study of shockwave interaction. Table 12 tabulates the lowest and highest C_D values recorded among the eight configurations for both BSCW and FSCW.

Figures 11 and 12 present the shockwave interaction through pressure coefficient contour plots and Q-criterion for configurations 4, 5, and 6. We observe that in both BSCW and FSCW configurations the intensity of shockwave interaction is reduced when the C-winglet has a large cant angle of 60°, large sweep angle of 60° and low taper ratio of 0.562 as illustrated in Figure 11a and Figure 12a compared to Figure 11b and Figure 12b where the intensity of the shockwave interaction is larger. This observation is consistent with the findings from the previous study (Guerrero et al., 2020). Although their study focused on a winglet configuration, it still provides valuable insights into shockwave interactions, particularly concerning the vertical section of the C-winglet configuration. In the case of the horizontal section of the C-winglet configuration, it offers similar advantages in terms of cant angle, sweep angle, and taper ratio, but to minimize shockwave interactions, the angle between the vertical and horizontal winglet sections should be 90° instead of 100°. Even though a low taper ratio of 0.562 for the C-winglet proves effective in reducing the size of the shockwave compared to a taper ratio of 1, Figure 11b demonstrates that other geometric parameters of the C-winglet can also impact the benefits of a smaller taper ratio. The benefit of having a large cant angle of 60° for the C-winglet, it helps to reduce the pressure differential between the upper and lower surface of the C-wing configurations. This reduction of the pressure differential has a positively influence by reducing the wave drag or shockwave intensity and wingtip vortices of the C-wing configurations.
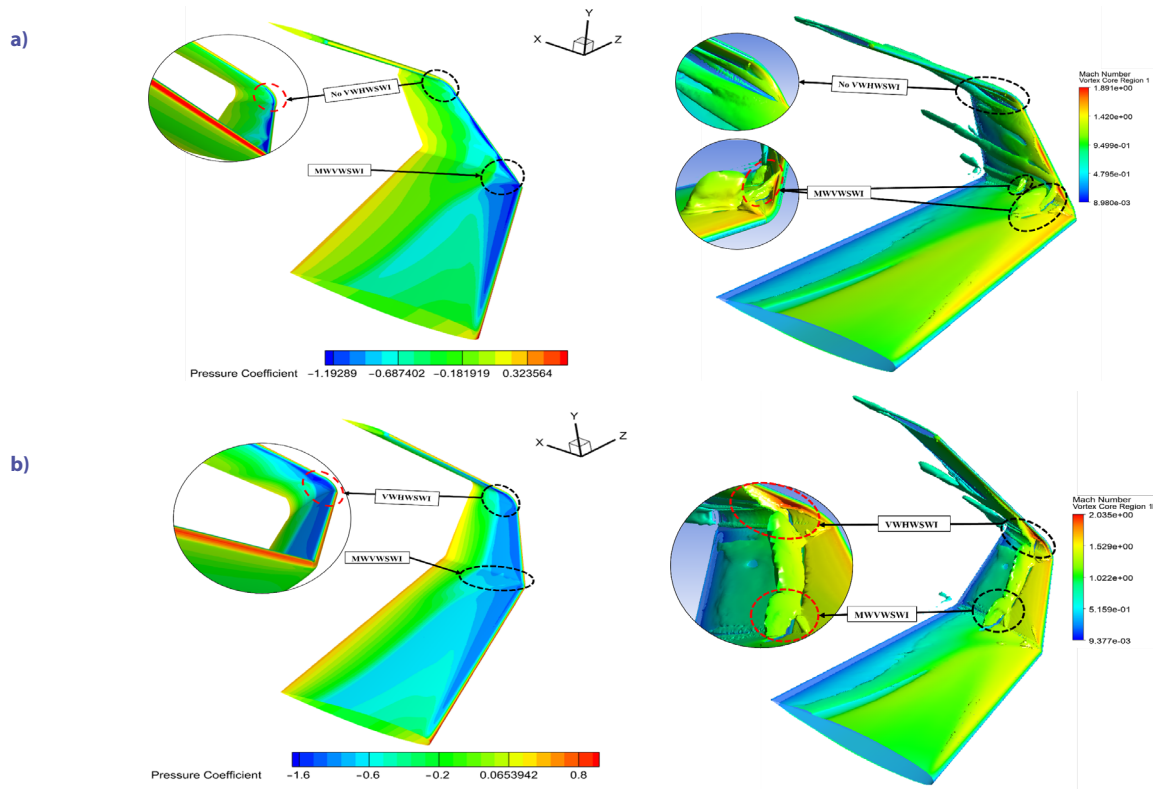

Pressure Coefficient   −1.19289   −0.687402   −0.181919   0.323564

Figure 10. Illustration of the geometric parameters for a C-wing configuration (with reference to configuration 4 of the BSCW configurations)

Figure 11. Shockwave interaction on BCSW configuration at Ma = 0.8395 and 3.06˚ AoA in terms of C_p (Above) and Q-criterion (Below): (a) Configuration 4; (b) Configuration 5. The Q-criterion illustrates the location and size of the shockwave interaction formed on the C-wing surface
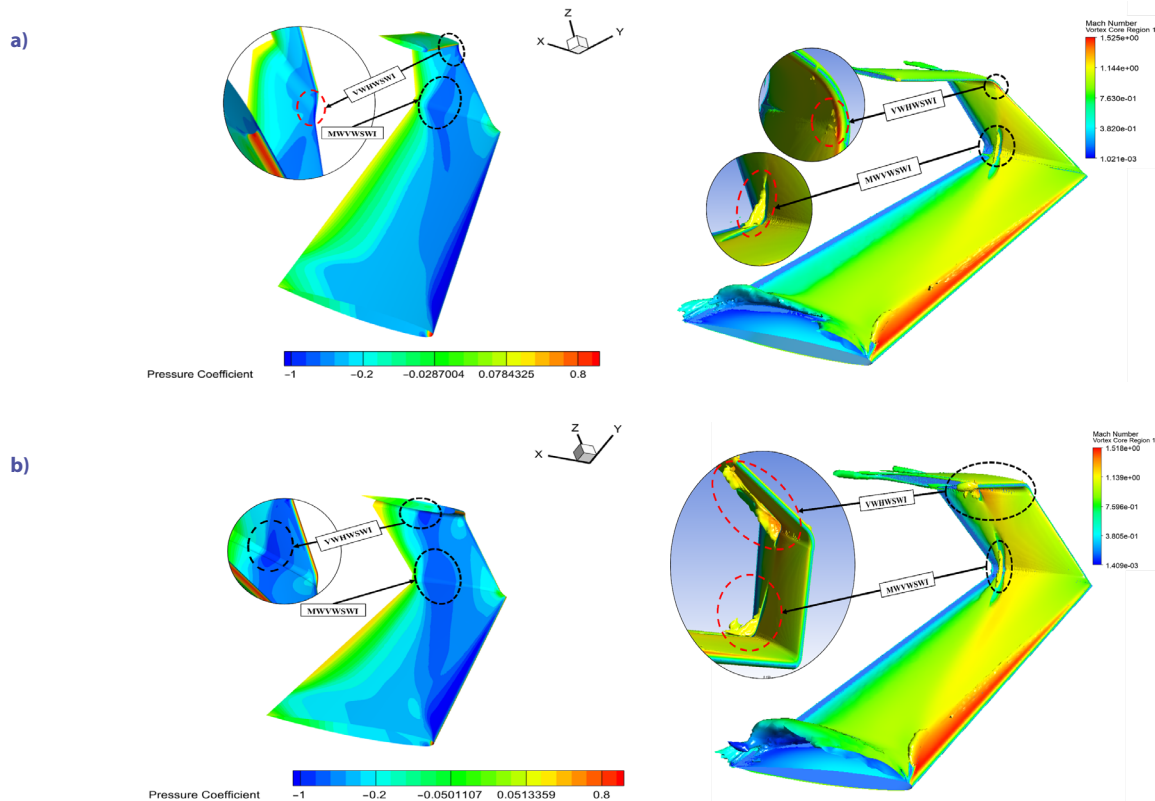

Figure 12. Shockwave interaction on FCSW configuration at Ma = 0.8395 and 3.06˚ AoA in terms of C_p (Above) and Q-criterion (Below): (a) Configuration 4; (b) Configuration 6. The Q-criterion illustrates the location and size of the shockwave interaction formed on the C-wing surface

4. Conclusions

The aerodynamic characteristics of backward and forward-swept wings with and without C-wing at 3.06° AoA and Ma = 0.8395 were investigated using both DoE and CFD. The ONERA M6 wing, a well-documented benchmark, and its computational domain were employed to evaluate the aerodynamic performance following best practices in the literature. Mesh 3 was selected based on the mesh convergence study. The C_p distribution graph along seven stations on the wingspan of a BSW (Backward-Swept Wing) configuration exhibits a similar trend between CFD data and experimental data. A ¼ fractional factorial DoE analysis was conducted to study C_L, C_D, and C_L/C_D for each of the eight BSCW and FSCW configurations, and significant factors were identified through normal plots. Additionally, the reduction models effectively retained essential factors without compromising the accuracy and offering insights for optimizing the C-winglet configurations in terms of C_L, C_D, and C_L/C_D. The aerodynamic performance and effect of shockwave interaction of the C-wing configurations were obtained from the CFD analysis. The numerical results show that by retrofitting the wing with C-winglet, the aerodynamic performance is significantly improved by approximately 9.38% and 9.74% for the BSCW and FSCW configurations, respectively, compared to wings without C-winglets. Among the eight configurations, configuration 4 of the BScCW and configuration 5 of the FSCW exhibited better aerodynamic efficiency than the other seven configurations. Another crucial aerodynamic characteristic was the shockwave interactions on the C-wing configurations, which negatively affect drag. These phenomena can be mitigated by modifying the geometry of the C-winglet for the respective wing configurations. Based on the results, configuration 4 for both the BSCW and FSCW configurations show a reduction in the drag coefficient and lower shockwave interaction, as indicated by the low-pressure region observed on the C-winglet in the pressure contour plot. Additionally, the Q-criterion was used to visualize the location and size of the shockwave interaction on the C-wing surface. To minimize shockwave interaction, these geometric factors were considered. First, a high ϕ_c combined with a low γ helped to reduce the pressure differential between the upper and lower surfaces of the C-winglet, resulting in a decrease of the shockwave intensity. Second, increasing the sweep angle contributes to a reduction in both skin friction drag, and interference drag on the surfaces of the C-winglet. Lastly, utilizing a low taper ratio of 0.562 effectively reduced the parasite drag on the C-winglet surface. However, a low taper ratio still can increase the size of the shockwave interaction due to influence of the other geometric parameters. In conclusion, this study highlights the significant influence of C-winglet geometry on the aerodynamic characteristics of both backward and forward-swept wing configurations. Through a combination of DoE and CFD, valuable insights for optimizing C-winglet configurations, enhancing aerodynamic performance, and mitigating the effect of shockwave interactions are provided, and ultimately advancing the field of aircraft design.

Future recommendation

This study highlights the importance of optimizing C-wing configurations at transonic speed. However, there are several aspects that can be considered in future work, including incorporating additional geometric parameters for the C-winglet, exploring the effect of subsonic and supersonic speeds, considering a wider range of angles of attack, conducting structural analysis on the C-wing configuration by focusing on the effect of shockwave interaction, examining the impact of different turbulence models on boundary layer separation and shockwave interaction predictions, utilizing supercritical aerofoils for C-wing design. By addressing these aspects in future research, a deeper understanding of C-wing configurations and their optimization potential can be achieved, leading to improved aerodynamic performance in different flight regimes.

Author contributions

Heershikesh Heerish Samputh: Writing – original draft, Investigation, Conceptualization, Methodology, Software, Data analysis. Lip Kean Moey: Data curation, Visualization, Supervision, Project administration. Vin Cent Tai: Conceptualization, Methodology, Software, Validation, Formal analysis. Yong Chai Tan: Writing – review & editing, Resources.

Disclosure statement

The Authors declare that there is no conflict of interest.

References

Antony, J. (2023). *Design of experiments for engineers and scientists*. Elsevier.

Balan, A., Park, M. A., Anderson, W. K., Kamenetskiy, D. S., Krakos, J. A., Michal, T., & Alauzet, F. (2020). Verification of anisotropic mesh adaptation for turbulent simulations over ONERA M6 wing. *AIAA Journal, 58*(4), 1550–1565. https://doi.org/10.2514/1.J059158

Bikkannavar, K., & Scholz, D. (2016). Investigation and design of a C-Wing passenger aircraft. *INCAS Bulletin, 8*(2), Article 2. https://doi.org/10.13111/2066-8201.2016.8.2.3

Coelho Barbosa, F. (2023). *Aircraft aerodynamic technology review – A tool for aviation performance and sustainability improvement* (SAE Technical Paper 2022-36-0022). SAE International. https://doi.org/10.4271/2022-36-0022

Das, A. K., & Dewanjee, S. (2018). Optimization of extraction using mathematical models and computation. In *Computational phytochemistry* (pp. 75–106). Elsevier. https://doi.org/10.1016/B978-0-12-812364-5.00003-1

Gagnon, H., & Zingg, D. W. (2016). Aerodynamic optimization trade study of a box-wing aircraft configuration. *Journal of Aircraft, 53*(4), Article 4. https://doi.org/10.2514/1.C033592

Gobpinaath, M., Sivajiraja, K., Suresh, C., & Ramesh, K. (2016). Design and analysis of non-planar wing in commercial aircraft. *International Journal of Innovations in Engineering and Technology*, *7*(3), Article 3.

Grimme, W., Maertens, S., & Bingemer, S. (2021). The role of very large passenger aircraft in global air transport – a review and outlook to the year 2050. *Transportation Research Procedia*, *59*(4), 76–84. https://doi.org/10.1016/j.trpro.2021.11.099

Guerrero, J. E., Sanguineti, M., & Wittkowski, K. (2020). Variable cant angle winglets for improvement of aircraft flight performance. *Meccanica*, *55*, 1917–1947. https://doi.org/10.1007/s11012-020-01230-1

Guerrero, J., Sanguineti, M., & Wittkowski, K. (2018). CFD study of the impact of variable cant angle winglets on total drag reduction. *Aerospace*, *5*(4), Article 126. https://doi.org/10.3390/aerospace5040126

Hrúz, M., Pecho, P., Bugaj, M., & Rostáš, J. (2022). Investigation of vortex structure behavior induced by different drag reduction devices in the near field. *Transportation Research Procedia*, *65*, 318–328. https://doi.org/10.1016/j.trpro.2022.11.036

International Air Transport Association. (2023). *Global outlook for air transport: Highly resilient, less robust*. IATA.

Jemitola, P., & Okonkwo, P. (2023). An analysis of aerodynamic design issues of box-wing aircraft. *Journal of Aviation Technology and Engineering*, *12*(2), 15–24. https://doi.org/10.7771/2159-6670.1253

Kazim, A. H., Malik, A. H., Ali, H., Raza, M. U., Khan, A. A., Aized, T., & Shabbir, A. (2022). CFD analysis of variable geometric angle winglets. *Aircraft Engineering and Aerospace Technology*, *94*(2), 289–301. https://doi.org/10.1108/AEAT-10-2020-0241

Kehayas, N. (2021). An alternative approach to induced drag reduction. *Aviation*, *25*(3), 202–210. https://doi.org/10.3846/aviation.2021.15663

Krishnan, S. G., Ishak, M. H., Nasirudin, M. A., & Ismail, F. (2020). Investigation of aerodynamic characteristics of a wing model with RGV winglet. *Journal of Aerospace Technology and Management*, *12*. https://doi.org/10.5028/jatm.v12.1108

Kroo, I. (2005). Nonplanar wing concepts for increased aircraft efficiency. *VKI Lecture Series on Innovative Configurations and Advanced Concepts for Future Civil Aircraft.* https://lf5422.com/wp-content/uploads/2014/08/vki_nonplanar_kroo-1.pdf

Le Quéré, C., Jackson, R. B., Jones, M. W., Smith, A. J., Abernethy, S., Andrew, R. M., De-Gol, A. J., Willis, D. R., Shan, Y., & Canadell, J. G. (2020). Temporary reduction in daily global CO2 emissions during the COVID-19 forced confinement. *Nature Climate Change*, *10*(7), 647–653. https://doi.org/10.1038/s41558-020-0797-x

Li, M.-F., Tang, X.-P., Wu, W., & Liu, H.-B. (2013). General models for estimating daily global solar radiation for different solar radiation zones in mainland China. *Energy Conversion and Management*, *70*, 139–148. https://doi.org/10.1016/j.enconman.2013.03.004

Rumsey, C. L., & Vatsa, V. N. (1995). Comparison of the predictive capabilities of several turbulence models. *Journal of Aircraft*, *32*(3), Article 3. https://doi.org/10.2514/3.46749

Schmitt, V. (1979). Pressure distributions on the ONERA M6-wing at transonic mach numbers, experimental data base for computer program assessment (*AGARD AR-138*). Advisory Group for Aerospace Research and Development.

Suresh, C., Ramesh, K., & Paramaguru, V. (2015). Aerodynamic performance analysis of a non-planar C-wing using CFD. *Aerospace Science and Technology*, *40*, 56–61. https://doi.org/10.1016/j.ast.2014.10.014

Sutthison, D., Wongkamchang, P., & Sukuprakarn, N. (2022). *Aerodynamic Studies of Small Box-Wing Unmanned Aerial Vehicle Using CFD*. Journal of Physics: Conference Series, *2235*(1), Article 012070. https://doi.org/10.1088/1742-6596/2235/1/012070

Whitcomb, R. T. (1976). *A design approach and selected wind tunnel results at high subsonic speeds for wing-tip mounted winglets*. NTRS – NASA Technical Reports Server.

Yahyaoui, M. (2019). A Comparative aerodynamic study of non-planar wings. *International Journal of Aviation, Aeronautics, and Aerospace*, *6*(4), Article 10. https://doi.org/10.15394/ijaaa.2019.1383

Zhou, Q., Shao, X., Jiang, P., Gao, Z., Wang, C., & Shu, L. (2016). An active learning metamodeling approach by sequentially exploiting difference information from variable-fidelity models. *Advanced Engineering Informatics*, *30*(3), 283–297. https://doi.org/10.1016/j.aei.2016.04.004

Notations

AoA – Angle of attack;

$b/2$ – Semi-span;

BSCW – Backward swept C-wing;

BSW – Backward swept wing;

C_D – Drag coefficient;

C_{D_r} – Regression equation for Drag coefficient;

C_L – Lift coefficient;

C_L/C_D – Lift to drag ratio;

C_{L_r} – Regression equation for Lift coefficient;

C_{L_r}/C_{D_r} – Regression equation for Lift to drag ratio;

C_p – Pressure coefficient;

DoE – Design of Experiment;

FSCW – Forward swept C-wing;

FSW – Forward swept wing;

Ma – Mach Number;

P – Pressure;

RRMSE – Relative Root Mean Square Error;

S – Sutherland constant;

T – Temperature;

T_0 – Reference temperature;

ϕ_c – Cant angle;

Λ_{vw} – Sweep angle of vertical winglet;

β_{hw} – Sweep angle of horizontal winglet;

γ – Angle between the vertical winglet and horizontal winglet;

λ_{CWt} – Taper ratio of C-winglet;

μ_0 – Reference viscosity.